Kuwait J. Sci. **45 (2)** pp 53-63, 2018

Novel synthesis of crystalline mesoporous tin dioxide doped with nanogold

Tariq Aqeel[1,*], Heather F. Greer[2], Ali Bumajdad[3]

[1]*Dept. of Science, College of Basic Education, The Public Authority of Applied Education and Training (PAAET), P.O. Box 23167, Safat 13092, Kuwait*

[2]*EaStCHEM, School of Chemistry, University of St Andrews, Purdie Building, St Andrews, KY16 9ST, United Kingdom*

[3]*Dept. of Chemistry, Faculty of Science, Kuwait University, P.O. Box 5969, Safat 13060, Kuwait*

**Corresponding author: tm.aqeel@paaet.edu.kw*

Abstract

We report the successful synthesis of a new material, a crystalline mesoporous tin dioxide (m-SnO_2) framework that contains nanogold clusters (m-SnO_2-Au), prepared using a direct soft method under ambient pressure. The structure, bulk, and surface properties of this new material are analyzed and confirmed by N_2 adsorption–desorption analysis, powder X-ray diffraction (XRD), high resolution transmission electron microscopy (HRTEM), energy dispersive X-ray (EDX), X-ray photoelectron spectroscopy (XPS), and UV-Vis spectroscopy. The material possesses a high Brunauer–Emmett–Teller (BET) surface area of 97 m^2g^{-1}, a narrow pore size distribution (2.1 to 3.3 nm) with an average pore diameter of 2.7 nm, and an average pore volume of 0.06 cm^3g^{-1}. We believe that the nanogold clusters initially occupy the pores of the mesoporous tin dioxide, thus restricting their growth before diffusing into the walls of tin dioxide during the second heat treatment. The median nanogold cluster size is 1.4 nm, indicating that this method controls both the porous structure and the size of the cluster within. The synthesized m-SnO_2-Au material has a relatively small bandgap of 3.0 eV, as determined using the Kubelka-Munk function. The UV-Vis and white-light optical sensitivities of m-SnO_2-Au are considerably higher than those of the parent material m-SnO_2.

Keywords: Doping; mesoporous tin dioxide; nanogold clusters; optoelectronic activity; soft templating synthesis.

1. Introduction

Tin dioxide is a semiconductor material with a wide bandgap of 3.6 eV (Aswaghosh *et al*., 2016; Popescu *et al*., 2001; Shaalan *et al*., 2016) that is employed in many applications; for example, in gas or vapor sensing (Wagner *et al*., 2011; Li *et al*., 2012; Tonezzer & Hieu, 2012; Brunet *et al*., 2012; Chen *et al*., 2013) and in the determination of optical sensitivity (Huang *et al*., 2014; Yu *et al*., 2011; Ganose & Scanlon, 2016). It is known that the bandgap of a semiconductor can be tuned by doping it with other elements (Aswaghosh *et al*., 2016; Yu *et al*., 2011; Ganose & Scanlon, 2016; Morris *et al*., 2001; Manikandan *et al*., 2016), by creating more oxygen defects (Aswaghosh *et al*., 2016; Manikandan *et al*., 2016), or by changing the crystal size (Aswaghosh *et al*., 2016; Manikandan *et al*., 2016; Brus, 1984; Smith & Nie, 2011). On the other hand, producing mesoporous tin dioxide increases the surface area of the material from 30 m^2g^{-1}, as a non-porous material (Benhebal *et al*., 2011), to about 100 m^2g^{-1} (Aqeel *et al*., 2016), depending on the heat treatment used. SnO_2 crystals increase in size as a result of heat treatment (Diéguez *et al*., 1996; Tunstall *et al*., 1999; Zhang & Liu 2000; Dieguez *et al*., 1996; Tunstall *et al*., 1999). This effect collapses the pores (the weakest part of the structure), thus decreasing the surface area at temperatures above 350 °C until the product eventually becomes flattened and nonporous (Severin *et al*., 1998). By creating a high surface area and decreasing the crystal size of the walls, the exposed contact surface area of the material increases, thereby leading to improvements in surface sensitivity, catalytic activity, and sorption ability. Nevertheless, introducing and maintaining the porosity of tin dioxide at multiple elevated temperatures has proved to be a challenging task (Aqeel *et al*., 2016).

A nanocluster size of 1 to 5 nm is important in order to induce quantum-effect properties and generate active surfaces (Gutierrez-Wing *et al*., 1997; Nancy-Xu *et al*., 2004). The surface plasmon behavior of nanogold clusters depends on various factors such as cluster size, the distances between clusters, and the substrate or matrix effect (Nancy-Xu *et al*., 2004; Okamoto & Yamaguchi, 2003). However, controlling the size of gold clusters without the use of inhibitors, such as micelles, surfactants, or organic compounds is rather difficult (Nancy-Xu *et al*., 2004; Gutierrez *et al*., 1999; Woehrle *et al*., 2002; Kumar *et al*., 2007). These inhibitors segregate the gold precursor, especially during wet chemistry processes, and minimize the aggregation of clusters when subjected to elevated heat treatment above 200 °C.

Previously, we reported a novel synthesis of mesoporous tin dioxide (m-SnO_2) that maintains its porosity and high surface area after being subjected to multiple heat treatments

at temperatures of up to 500 °C (Aqeel *et al*., 2016). This feature enables post-cluster synthesis to be applied to the porous material, which requires further heat treatment. This procedure was employed in this work to produce m-SnO_2, with nanogold (Au) particles introduced by post synthesis. The post synthesis of Au was performed after ensuring that the pores had opened and were free or partially free of surfactant materials by extended Soxhlet extraction, followed by calcination to further remove remaining surfactants and strengthen the m-SnO_2 framework by condensation. Evacuation of the pores enhances diffusion of the Au precursor through the pores, while the pores segregate and limit the aggregation of Au particles during heat treatment. Such pores can be considered as nucleation sites that are utilized to restrict the growth of any guest clusters, in this case nanogold clusters, by the confinement effect. In addition, the inclusion of a reducing gas, such as H_2, is essential for the conversion of the Au precursor into its metallic form below room temperature; it also limits aggregation during heat treatment, since nanogold can sinter at temperatures as low as 330 °C, (Goudeli & Pratsinis, 2016). We found that this material is active in both the UV and the visible spectral region, and its optoelectronic activity increases significantly after the introduction of nanogold clusters into the m-SnO_2. The present findings suggest that m-SnO_2-Au may be employable as an optical catalyst for the photo-degradation of organic compounds such as phenol and its derivatives in water (Benhebal *et al*., 2013; Fatimah *et al*., 2015; Abdullah *et al*., 2016; Asiri *et al*., 2011; Aqeel & Bumajdad, 2017). It is known that phenol and its derivatives are toxic to both marine life and humans. These molecules are usually found in waste water that can be discharged or leaked into water resources (Ritson *et al*., 2014; Smith *et al*., 2015; Bakke *et al*., 2013). With this in mind, m-SnO_2-Au could be employed as an integral component of optoelectronic devices such as photovoltaic cells (Chen *et al*., 2013; Yu *et al*., 2011; Ganose & Scanlon, 2016; Fuchs *et al*., 2011), for the labeling of antigens and amino acids (Sawada *et al*., 2000; Loukanov & Gagov, 2012), to decrease heat transfer through glass by coating with SnO_2-Au (Chowdhury *et al*., 2005), and for harvesting of solar energy like plants using quantum-sized gold clusters (Magis *et al*., 2010). It is well known that the future of humanity rests on sustainable clean energy resources.

In this work, we demonstrate that the introduction of nanogold clusters into m-SnO_2 improves the electrical and optical properties of the final product in comparison to the parent m-SnO_2.

2. Experimental

2.1 Synthesis

2.1.1 Preparation of mesoporous SnO_2

Mesoporous SnO_2 was prepared by slowly stirring hexadecylamine (Alfa Aesar, analytical grade, 90%) (0.26 g) in ^{i}PrOH(Alfa Aesar, 99%) (24.4 cm^3) until completely dissolved (colorless transparent solution was attained). Next, $Sn(O^{i}Pr)_4$ (Alfa Aesar, 99%) (1.9 g) was added to the solution at room temperature such that the surfactant: solvent: Sn molar ratio was 0.2:60:1.0 (Aqeel *et al*., 2016). The reactants were stirred slowly under water-saturated air (approximately 80% humidity) at atmospheric pressure for 3 days. The obtained product was filtered and washed with deionized water and ethanol (Sigma Aldrich, 99.8%). The product was subsequently transferred to a Soxhlet extractor and extracted with ethanol overnight (approximately 16 h), in order to remove the surfactant, and was subsequently collected by filtration. The product was calcined at 300 °C for 2 h in air (heating rate of 2 °C min^{-1}). A portion of the synthesized m-SnO_2 (0.3 g) was dehydrated at 120 °C for 3 h under N_2 (grade 6, 99.9999%). $NaAuCl_4$ (Alfa Aesar, 99.99%) (0.005g) was dissolved in methanol (4.5 cm^3) (HPLC grade 99.9%) at 0 °C and then mixed with the dehydrated-SnO_2 for 30 min under N_2. Subsequently, 2% H_2 in N_2 was introduced at room temperature until dryness. Finally the sample was heat-treated at 400 °C for 10 min under 2% H_2 in N_2, followed by cooling to room temperature under ambient air (heating rate of 3 °C min^{-1}). The H_2 gas was used to reduce the Au precursor by transforming it into metallic Au. The concentration of H_2 gas in N_2 is recommended to be under 5% to prevent explosions at elevated temperatures. All chemicals were used as received, without further purification.

2.2 Characterization

Powder X-ray diffraction (XRD) measurements were performed using a Bruker AXS D8 ADVANCE diffractometer with a copper target (λ = 1.5418 Å); the DIFFRAC^{plus} software was used for analysis, and the following operational parameters were employed: 40 kV; 40 mA; front slit window size 0.1 mm for low angle, 1.0 mm for wide angle scans; the deflection plate was placed at a distance of 0.5–1.0 mm above the sample for the low angle scan; continuous coupled two-theta scan/theta scan mode, 0.5 step/s. Nitrogen gas adsorption–desorption measurements were performed using a Micrometrics Tristar analyzer. High resolution transmission electron microscopy (HRTEM) imaging was performed using a JEOL JEM-2011 electron microscope operating at 200 kV. The images

were recorded using a Gatan 794 CCD camera. ImageJ software was used to analyze the TEM images. The TEM instrument was equipped with an Oxford Link ISIS Semi STEM energy dispersive X-ray diffraction (EDX) system, which was used for determining the chemical compositions of the samples. X-ray photoelectron spectroscopy (XPS) measurements were performed using a Thermo ESCALAB 250Xi spectrometer with a monochromator and an Al-Kα radiation source (1486.6 eV). The spectra were recorded and processed using an Avantage data system. The analyses were carried out using the following parameters: analysis chamber pressure of 10^{-9} Torr, step size of 0.1 eV, dwell time of 100 ms, and pass energy of 20 eV. All binding energy values were determined with respect to the C1s line (284.6 eV) originating from adventitious carbon. A flood gun was used in the standard charge compensation mode to neutralize the charge buildup on the surface of the insulating layer. Optical activation experiments were performed using an ENERGETIQ white laser-driven light source (LDLS). The distance was set to 7 cm (20–200 mWm^{-2}), and the UV source was an Hg tube lamp (24 W, 365 nm, 230 V, and 50–60 Hz) purchased from UniEquip. The current was measured at room temperature using an Agilent B2901A source/measure unit and two banana probes placed 4 mm apart. UV-Vis spectroscopy was performed using a Cary 5000 UV-Vis-NIR spectrophotometer (Version 1.12) with the following settings: abs mode 200–800 nm, scan rate 600.000 nm min^{-1}, data interval 1.000 nm, full slit height, double beam mode, signal to noise mode off, and baseline correction on.

3. Results and discussion

3.1. X-Ray diffraction

The low-angle XRD patterns of m-SnO_2 before and after the introduction of nanogold clusters (m-SnO_2-Au) are presented in Figure 1. The patterns clearly reveal that the main <100> diffraction peaks did not shift for both samples. Figure 1(a) shows the XRD pattern of mesoporous SnO_2 calcined at 300°C after the pores were evacuated of the templating material by Soxhlet extraction followed by calcination. Figure 1(b) shows that the mesoporous structure of m-SnO_2 remained intact after the synthesis of the nanogold clusters within its pores and the subsequent heat treatment, which was performed at 400 °C under H_2/N_2 to reduce the introduced gold precursor to metallic gold. The decrease in the intensity of the main diffraction peak associated with m-SnO_2-Au, relative to that of m-SnO_2 (Figure 1(b)), indicates that some

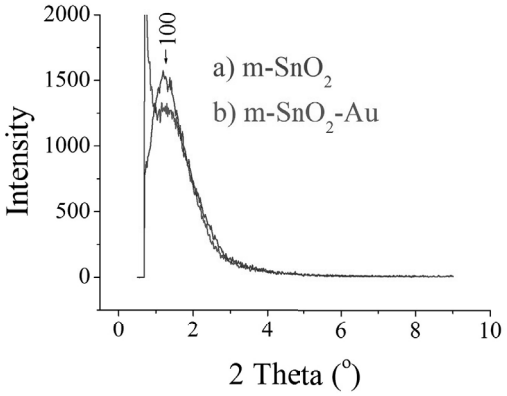

Fig. 1. Low-angle XRD patterns for a) m-SnO_2 calcined at 300 °C, and b) after nanogold clusters were synthesized within the pores of the m-SnO_2, followed by a second heat treatment at 400 °C.

pores were occupied by nanogold clusters; further evidence includes the observed decrease in the total surface area and pore volume, as detailed in the results of the N_2 sorption measurements, below. The *d*-spacing of the m-SnO_2-Au material was calculated from the low-angle XRD spectrum in Figure 1(b) and was found to be 68.0 Å. Furthermore, the distance between the centers of two adjacent pores (a_0) was found to be 78.5 Å. By subtracting the average pore size (27.0 Å), as determined from the N_2 sorption measurements (see Figure 3(d)), from this value, the average wall thickness was determined to be 51.5 Å; the HRTEM images in Figure 5(b) confirm that the SnO_2 crystal size was approximately 50 Å.

The wide-angle XRD patterns for m-SnO_2-Au and m-SnO_2, presented in Figure 2 confirm the crystalline nature of the samples; the structures of these materials were assigned to cassiterite SnO_2, in good agreement with JCPDS card 01-077-0447 (Aqeel *et al*., 2016). The peak intensities for m-SnO_2-Au (Figure 2(b)) were higher compared to those of m-SnO_2 (Figure 2(a)).

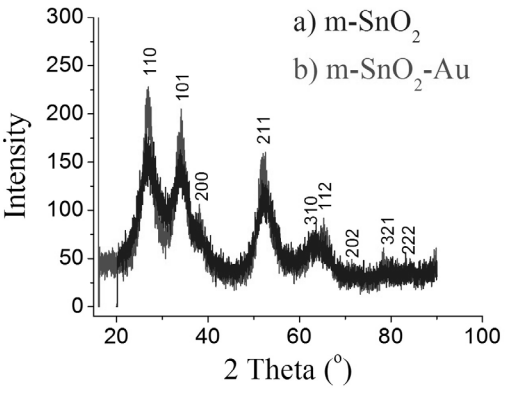

Fig. 2. Wide-angle XRD patterns of a) m-SnO_2, and b) m-SnO_2-Au samples.

The difference in peak intensity can be attributed to the fact that the m-SnO_2-Au sample underwent two successive heat treatments, first at 300 °C, to strengthen the framework through further condensation and to remove any remaining organic templating material, and then at 400 °C to convert the Au precursor into nanometallic Au; whereas m-SnO_2 was calcined only once at 300 °C. Moreover, the broad diffraction peaks indicate that the m-SnO_2 crystals are small in size. By contrast, the nanogold clusters were too small, too few in number, and did not have regular repeating distances that could be detected by wide-angle XRD. Therefore, other methods such as XPS and EDX were used to detect and analyze the nanogold clusters.

3.2. N_2 adsorption–desorption measurements

N_2 sorption measurements were performed to determine the average pore sizes, average pore volumes, and total surface areas of the m-SnO_2-Au and m-SnO_2 materials. Figures 3(a) and 3(c) depict typical type-IV isotherms that are representative of mesoporous materials (Sing *et al*., 1985). Each isotherm can be divided into three main sections. The first section starts at the beginning of the isotherm, in the low-pressure region, and extends to the first point of inflection (just before a relative pressure of 0.2). This region corresponds to the start of monolayer to multilayer adsorption within the pore walls. The second section, which extends from the first inflection point to the second one (between relative pressures of 0.2 and 0.6) corresponds to capillary condensation within the pores and is indicative of the mean pore diameter.

The last section of the isotherm is a flat section ranging between relative pressures of 0.6 and 0.9, and represents multilayered adsorption on the external surface after complete filling of all pores. A small hysteresis loop is observed in Figure 3(c) for m-SnO_2-Au, lying between types H1 and H2 according to the IUPAC classification (Sing *et al*.,1985), and was observed during the desorption cycle between relative pressures of 0.55 and 0.4, indicating the existence of different pore shapes and sizes in this material. A type-H1 hysteresis loop is indicative of cylindrical pores whereas an H2 loop represents irregular pore shapes (Sing *et al*., 1985).

The pore size distributions of the synthesized materials, shown in Figures 3(b) and 3(d), are narrow, confirming that the proposed synthesis method provides excellent control over the pores size. The pore sizes of the m-SnO_2-Au sample were in the 21–33 Å range, with an average size of 27 Å; these pore sizes are consistent with mesoporous materials, as classified by IUPAC (Sing *et al*., 1985). The BET surface area of the synthesized m-SnO_2-Au material was 97 m^2g^{-1}, with a pore volume 0.06 cm^3g^{-1}, as presented in Table 1. This surface area is relatively high considering that the material has been subjected to two heat treatments and has nanogold clusters occupying some of its pores. These results indicate that this material has maintained its mesoporosity even after the synthesis of nanogold particles within its pores and subsequent heat treatments at 400 °C. By contrast, the N_2 sorption results for the mesoporous m-SnO_2 that was

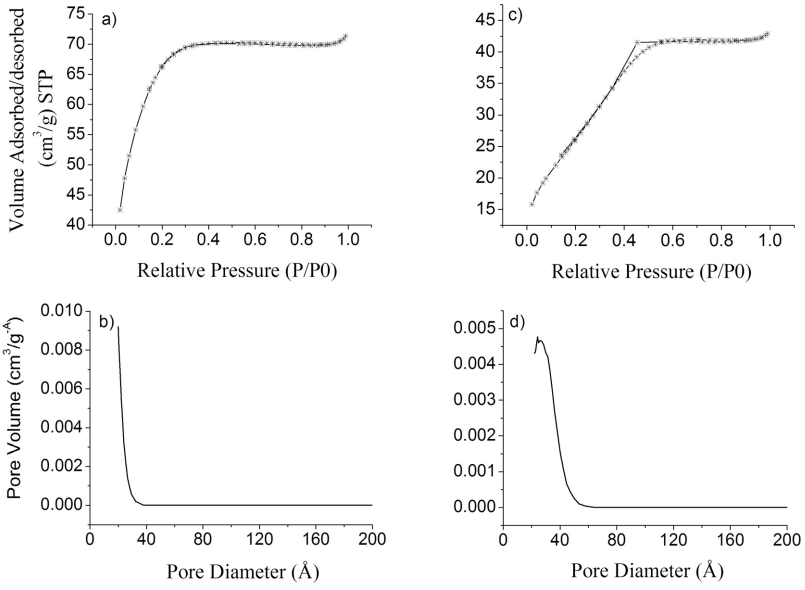

Fig. 3. N_2 adsorption–desorption isotherms for the mesoporous samples after the second heat treatment at 400 °C. a) m-SnO_2 and b) its pore-size distribution; c) m-SnO_2-Au and d) its pore-size distribution.

subjected to a similar procedure, but without the insertion of the nanogold, displayed a BET surface area and pore volume of 113 m^2g^{-1}, 0.07 cm^3g^{-1}, respectively, and a maximum pore size of 23 Å (Table 1).

The isotherm produced by m-SnO_2 did not show any hysteresis, indicating a more uniform pore shape and smaller pore size distribution. The decrease in the BET surface area from 113 to 97 m^2 g^{-1} might indicate that some of the nanogold clusters occupy the pores, which is in agreement with the decrease observed in the intensity of the main XRD peak, as shown in Figure 1(b).

3.3. X-ray photoelectron spectroscopy

The Sn and Au oxidation states in the sample, as well as the chemical linkages present, were investigated using XPS (Figure 4). The Sn peaks at 486.3 and 495.1 eV (Figure 4(a)) correspond to Sn^{4+} $3d_{5/2}$ and $3d_{3/2}$ orbital splitting, which indicate the formation of the tin dioxide framework (Uddin *et al*., 2012; Zhao *et al*., 2012). The absence of an XPS peak at 493.6, resulting from $3d_{3/2}$ orbital splitting caused by Sn–Au bonding, indicates that this type of bonding was not present. The oxygen XPS peak at 530.1 eV, which results from O1s orbital splitting, corresponds to O–Sn bonding in the SnO_2 framework. In addition, a smaller peak observed at 531.6 eV may indicate the existence of oxygen defects (vacancies) in the framework, and/or the presence of chemisorbed O^- or OH^- at the material surface/subsurface, in the form of tin-hydroxyl groups [$Sn(OH)_4$] (Uddin *et al*., 2012; Zhao *et al*.,2012) (see Figure 4(b)).

Table 1. Brunauer–Emmett–Teller (BET) surface areas, pore sizes, and pore volumes of m-SnO_2 and m-SnO_2-Au samples.

Sample	BET surface area (m^2g^{-1})	Average pore size (Å)	Pore volume (cm^3g^{-1})
m-SnO_2 (calcined at 300 °C)	222	20	0.1
m-SnO_2 (calcined at 400 °C)	113	23	0.07
m-SnO_2-Au (calcined at 400 °C)	97	27	0.06

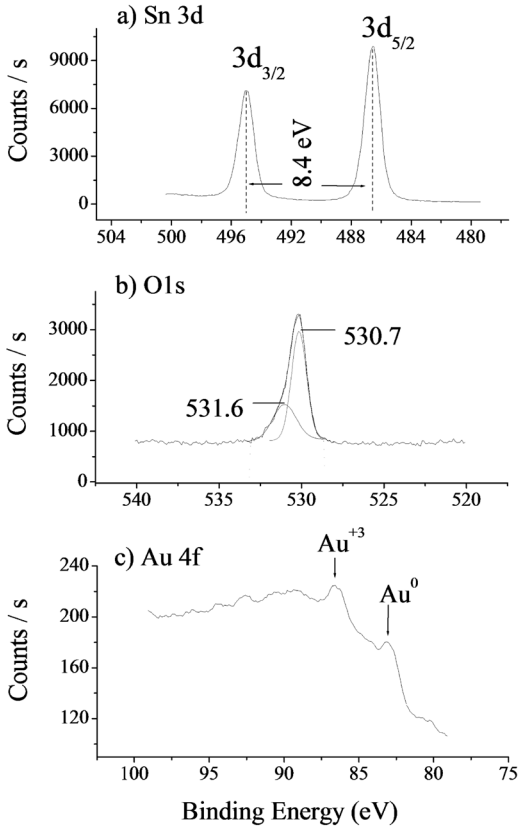

Fig. 4. XPS spectra of m-SnO_2-Au.

The XPS peak at 83.4 eV corresponds to Au $4f_{7/2}$ orbital splitting and indicates the existence of metallic gold (Rodriguez *et al*., 2014; Hostetler *et al*., 1998; Liu *et al*., 2013), whereas the XPS peak at 86.5 belongs to the Au $4f_{7/2}$ of ionic gold (Liu *et al*., 2013) and is indicated by the arrow in Figure 4(c). We believe that ionic gold comes from unreduced gold chloride precursor that has escaped the reducing heat treatment.The percentage weight of chloride (wt %) determined from the XPS 2p orbital at 197.9 eV is 0.7wt%. This Cl ion is believed to be associated with the ionic Au in the $NaAuCl_4$ precursor; when divided by 3, this amount becomes 0.2wt% when compared to the total amount of Au (3.5 wt % detected by EDX), and is thus equal to only 5% of the total gold present in the sample.

3.4. High-resolution transmission electron microscopy

HRTEM analysis was performed on the m-SnO_2-Au sample. Figure 5(b) shows an HRTEM image recorded from the edge of the particle whose TEM imageis shown in Figure 5(a); the crystal diffraction planes reveal that the lattice fringes match those of SnO_2 and the crystal sizes are within 5 nm. These crystal sizes are very similar to those calculated from the XRD pattern given in Figure 1 using the Scherrer equation.

Figure 5(d) shows the dark-field TEM image corresponding to that shown in Figure 5(c) and provides further detail about the overall distribution of nanogold clusters in the matrix (the bright spots). In addition, the image in Figure 5(f) clearly shows that the porosity of the structure is spread through the entire sample. Moreover, the pore sizes were determined to be in the range of 2.4 to 5 nm, with nanogold cluster sizes of 0.7–2.1 nm (measured using the ImageJ software). The Au clusters locations are inside and close to the pores, clearly indicating that they have diffused into the m-SnO_2 framework, as evidenced by the dark round spots at the left edges of Figure 5(f), inside the red rectangle and marked by the red lines and circles on the enlarged image, as well as in Figures 5(a) and 5(c). We suspect that diffusion has occurred during the heat treatment under the H_2/N_2 reducing gas at 400 °C. At this temperature, under reducing conditions, the gold precursor tends to form metallic nanogold clusters. However, the sizes of the clusters are restricted by the pore walls. It is thought that if the gold precursor

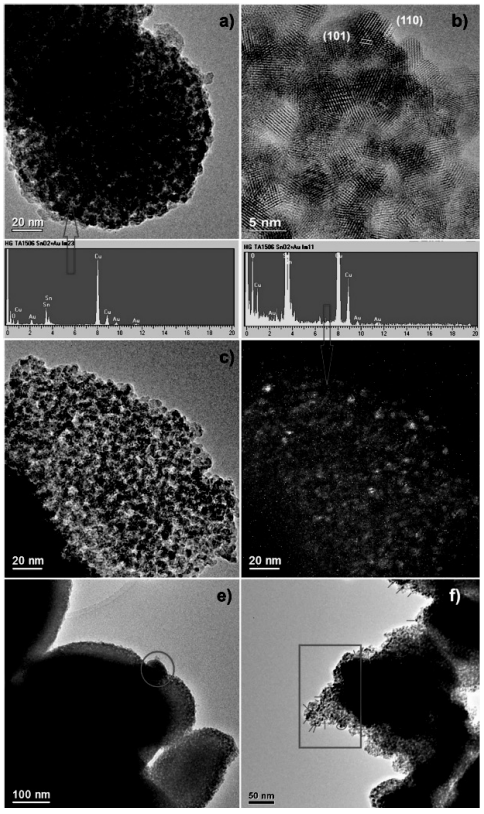

Fig. 5. TEM images of m-SnO_2-Au and the corresponding EDX spectra. a) TEM image showing the porous nature of m-SnO_2. b) HRTEM image recorded from a region shown in a) with the lattice fringes indexed to SnO_2. c, d) Bright- and dark-field TEM images of Au nanoparticles with mesoporous SnO_2. e) TEM image highlighting a large isolated nanogold cluster (circled). f) Image highlighting small nanogold clusters (inside the rectangle) that have diffused into the matrix.

existed initially outside of the pores, it would have aggregated to form larger clusters, such as the one indicated by the red circle in Figure 5(e); this cluster is around 55 nm in size. These results highlight the important role of porosity in restricting the size and growth of nanoclusters.

3.5. Energy dispersive X-ray diffraction

EDX measurements were performed on the sample to confirm its surface and near-surface compositions; two representative spectra are shown in Figure 5, clearly revealing the K-lines of O, and the L-lines of the Au and Sn atoms that exist in the material. The Cu K- and L-lines belong to the specimen grid. The total percentage weight of Au determined by EDX is 3.5%.

3.6. UV-Vis spectroscopy and optical sensitivity

3.6.1. UV-Vis diffuse reflectance transmission technique

The UV-Vis diffuse reflectance transmission (DRT) technique was employed to study both m-SnO_2 and m-SnO_2-Au samples and the corresponding spectra are presented in Figure 6(a). The m-SnO_2-Au sample exhibited a higher transmission than the m-SnO_2 sample. A Tauc plot was constructed using the data obtained by DRT to determine the bandgaps of these materials, employing the Kubelka-Munk function ($F_{(K-M)}$ (R)) as shown in the equation: $F_{(K-M)}$ (R) = $(1-R)^2/ 2R$, where R is the percentage of reflectance transition. A graph was constructed to directly determine the bandgaps by plotting [F(R)* E^2] against the photon energy (E) in electron volts (eV).

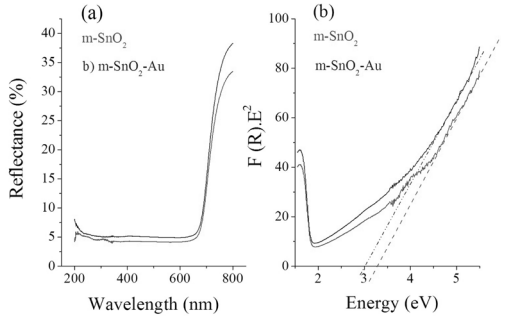

Fig. 6. (a) UV-Vis diffuse transmission reflection spectra, and (b) Tauc plots of the Kubelka-Munk function versus photon energy for the m-SnO_2 sample, and the m-SnO_2-Au sample, both calcined at 400 °C.

The bandgap (E_g) was determined by extrapolating the linear part of the curve to the intersection with the energy axis, as shown in Figure 6(b). The band gaps for m-SnO_2 and m-SnO_2-Au were determined to be 3.3 eV and 3.0 eV, respectively; both are considerably lower than the macrostructure value of 3.6 eV. A smaller bandgap could indicate the existence of oxygen defect sites, which form a new intermediate

density-of-state band that facilitates charge transfer at the metal–semiconductor interface (Manikandan *et al*., 2016). The contribution of nanogold plasmonic electrons that were excited by UV irradiation would have increased the electron density of the entire matrix (Chen *et al*., 2013; Huang *et al*., 2014; Ganose & Scanlon, 2016; Nancy-Xu *et al*., 2004; Okamoto &Yamaguchi, 2003).

3.6.2 Optical sensitivity

3.6.2.1. UV experiments

In these experiments, the samples were exposed to 320-nm UV light for 300 s, after which the UV source was extinguished and the sample was monitored for further 400 s; currents were measured over the entire 700 s of these experiments (Figure 7). For each sample, the current was observed to increase during the exposure to UV light, and then decrease once the UV source was extinguished. This behavior may indicate that the valance electrons were sufficiently excited to hop from the valance band to the conduction band as a result of the absorption of UV-light energy, thus crossing the bandgap barrier. The energy produced by the UV lamp was 3.8 eV, whereas the bandgaps measured for m-SnO_2 and m-SnO_2-Au samples were 3.3 and 3.0 eV, respectively. Moreover, the maximum current produced by m-SnO_2-Au was 850 μA (Figure 7), that is, more than 386 times higher than that produced by m-SnO_2 (2.2 μA) under the same experimental conditions. These results confirm that the bandgap of the m-SnO_2-Au sample is smaller than that of m-SnO_2 and that additional electrons may be produced by the nanogold (plasmonic effect) to increase the conductivity of the sample. This experiment verifies that both materials can be activated by UV energy.

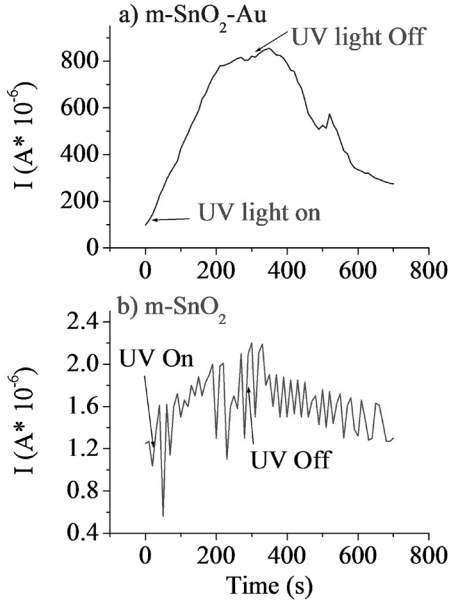

Fig. 7. Excitation of samples by UV light and the corresponding current measured on the surface of each sample: a) m-SnO_2-Au and b) m-SnO_2.

3.6.2.2. Visible white-light experiments

The optical sensitivity (optoelectronic activity) of the samples under visible white-light conditions was also investigated. The current produced by the samples during exposure to white light is shown in Figure 8. The m-SnO_2-Au sample produced a maximum current of 112 μA (Figure 8(a)), which is 70 times higher than that produced by the m-SnO_2 sample (1.6 μA, Figure 8(b)) under the same experimental conditions. This result confirms that these materials can also be excited by visible light and may be employable in

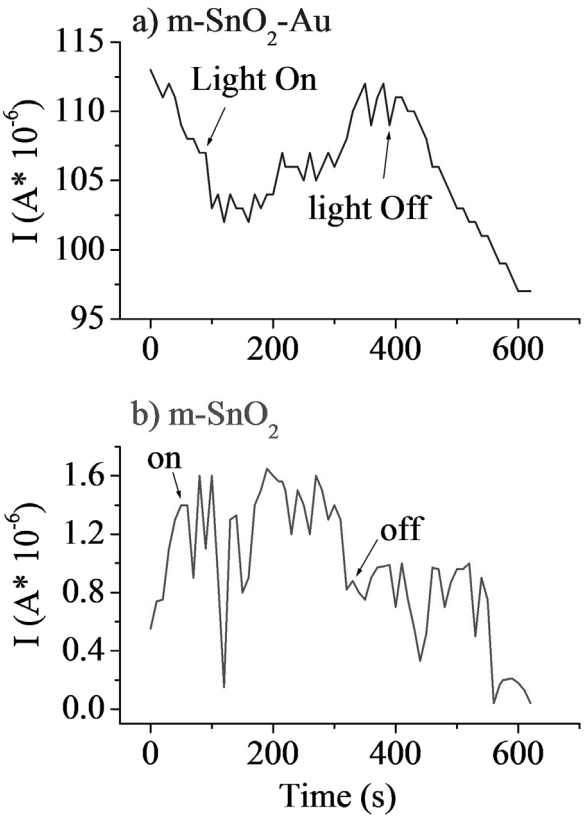

Fig. 8. Excitation of the samples by visible light and the corresponding current produced on the surface of each sample: (a) m-SnO_2-Au and (b) m-SnO_2.

4. Conclusions

A new crystalline mesoporous tin dioxide framework containing nanogold clusters (m-SnO_2-Au) was successfully synthesized. This new material has a BET surface area of 97 m^2g^{-1}, a mean pore size of 2.7 nm, and a pore volume 0.06 cm^3g^{-1}. Initially, following the post-treatment of porous SnO_2, the nanogold clusters occupied the pores of the mesoporous tin dioxide framework, which restricted their further growth. Some of these clusters subsequently diffused into the walls of the tin dioxide as a result of the heat treatment, as evidenced

by HRTEM. The average nanogold cluster was 1.4 nm in size. The m-SnO_2-Au sample exhibited a bandgap of 3.0 eV, which is narrower than that of m-SnO_2, as determined using the Kubelka-Munk function. The new material described is optically excited by both UV and visible light, and may find utility in both optical and electronic applications.

5. Acknowledgments

This project was supported and funded by the Public Authority of Applied Education and Training (PAAET: Project No. BE-13-08 entitled: Synthesis of Mesoporous Tin Dioxide Powder Stable above 400 °C) in collaboration with Kuwait University and Professor Duncan Bruce at the University of York (BET and XRD experiments). We acknowledge the support of the research administration of the Kuwait University, by providing the XPS (Project No. GS01/05) and UV-Vis instruments (No. GS01/10). We would like to acknowledge Professor Goran Pichlerofat Kuwait University for his assistance in using the LDLS instrument in his laboratory, and the TEM/EDX facilities at the University of St Andrews.

References

Abdullah, A. M., Al-Thani, N. J., Tawbi K. & Al-Kandari, H. (2016). Carbon/nitrogen-doped TiO_2: New synthesis route, characterization and application for phenol degradation, Arabian Journal of Chemistry, **9**:229–237.

Aqeel, T., Greer, H. F., Zhou, W., Bruce, D. W. & Bumajdad, A. (2016). Novel direct synthesis of mesoporous tin dioxide network intact up to 500 °C, Journal of Nano Research, **40**:79–89.

Aqeel, T. & Bumajdad, A. (2017). Use of mesoporous tin dioxide containing zinc oxide nanoparticles for degradation of phenol by sunlight, Science of Advanced Materials, **9**:1–10.

Asiri, A. M., Al-Amoudi, M. S., Al-Talhi, T. A. & Al-Talhi, A. D. (2011). Photodegradation of Rhodamine 6G and phenol red by nanosized TiO_2 under solar irradiation, Journal of Saudi Chemical Society, **15**:121–128.

Aswaghosh, L., Manoharan, D. & Victor Jaya, N. (2016). Defect structure and optical phonon confinement in ultrananocrystalline BixSn1-xO_2 (x = 0, 0.03, 0.05, and 0.08) synthesized by a sonochemical method, Physical Chemistry Chemical Physics, **18**:5995–6004.

Bakke, T., Klungsoyr, J. & Sanni, S. (2013). Environmental impacts of produced water and drilling waste discharges from the Norwegian offshore petroleum industry, Marine Environmental Research, **92**:154–169.

Benhebal, H., Chaib, M., Léonard, A., Lambert, S. D. & Crine, M. (2011). Synthesis, characterization and photocatalytic properties of alkali metals doped tin dioxide, Journal of Molecular Structure, **1004**, 222–226.

Benhebal, H., Chaib, M., Salmon, T., Geens, J., Leonard, A., *et al.* (2013). Photocatalytic degradation of phenol and benzoic acid using zinc oxide powders prepared by the sol–gel process, Alexandria Engineering Journal, **52**:517-523.

Brunet, E., Maier, T., Mutinati, G. C., Steinhauer, S., Köck, A., *et al.* (2012). Comparison of the gas sensing performance of SnO_2 thin film and SnO_2 nanowire, Sensors and Actuators B: Chemical, **165**:110–118.

Brus, L. E. (1984). Electron-electron and electron-hole interactions in small semiconductor crystallites: The size dependence of the lowest excited electronic state, Journal of Chemical Physics, **80**:4403–4409.

Chen, G., Seo, J., Yang, C. & Prasad, P. N. (2013). Nanochemistry and nanomaterials for photovoltaics, Chemical Society Reviews, **42**:8304–8338.

Chowdhury, H., Xu, X., Huynh, P. & Cortie, M. B. (2005). Radiative heat transfer across glass coated with gold nano-particles, Journal of Solar Energy Engineering, **127**:70–75.

Diéguez, A., Romano-Rodríguez, A., Morante, J. R., Weimar, U., Schweizer-Berberich, M., *et al.* (1996). Morphological analysis of nanocrystalline SnO_2 for gas sensor applications. Sensors and Actuators B Chem. **31**, 1–8.

Fatimah, I., Wijaya, K. & Narsito (2015). Microwave assisted preparation of TiO_2/Al-pillared saponite for photocatalytic phenol photo-oxidation in aqueous solution, Arabian Journal of Chemistry, **8**:228–232.

Fuchs, A., Schimper, H. J., Klein, A. & Jaegermann, W. (2011). Photoemission studies on undoped SnO_2 buffer layers for CdTe thin film solar cells, European Materials Research Society Conference Symp. Advanced Inorganic Materials and Concepts for Photovoltaics, Energy Procedia, **10**:149-154. Nice, France.

Ganose, A. M. & Scanlon, D. O. (2016). Band gap and work function tailoring of SnO_2 for improved transparent conducting ability in photovoltaics, Journal of Materials Chemistry C, **4**:1467–1475.

Goudeli, E. & Pratsinis, S. E. (2016). Crystallinity dynamics of gold nanoparticles during sintering or coalescence, AIChE Journal, **62**(2):589–598.

Gutierrez, E., Powell, R.D., Furuya, F. R.,Hainfeld, J. F., Schaa, T. G., *et al.* (1999). Green gold, a giant cluster compound of unusual electronic structure, The European Physical Journal, **D9**:647–651.

Gutierrez-Wing, C., Ascensio, J. & Jose-Yacaman, M. J. (1997). Isolation of smaller nanocrystal Au molecules: Robust quantum effects in optical spectra, The Journal of Physical Chemistry B, **101**:7885–7891.

Hostetler, M. J., Wingate, J. E., Zhong, C. J., Harris, J. E., Vachet, R.W., *et al.* (1998). Alkanethiolate gold cluster molecules with core diameters from 1.5 to 5.2 nm: core and monolayer properties as a function of core size, Langmuir, **14**:17-30.

Huang, B. J., Li, F., Zhang, C.W, Li, P. & Wang, P. J. (2014). Electronic structure and optical properties of Ag doped SnO_2 nanoribbons, Royal Society of Chemistry Advances, **4**:41819–41824.

Kumar, S. S., Kumar, C. S., Mathiyarasu, J. & Phani, K. L. (2007). Stabilized gold nanoparticles by reduction using 3,4-ethylenedioxythiophene-polystyrenesulfonate in aqueous solutions: Nanocomposite formation, stability, and application in catalysis, Langmuir, **23**:3401–3408.

Liu, J., Wang, F., Qi, S., Gua, Z. & Wu, G. (2013). Highly selective epoxidation of styrene over gold–silica catalysts via one-pot synthesis: synthesis, characterization, and catalytic application, New Journal of Chemistry, **37**:769–774.

Li, X., Cho, J. H., Kurup, P. & Gu, Z. (2012). Novel sensor array based on doped tin oxide nanowires for organic vapour detection, Sensors and Actuators B: Chemical, **162**:251–258.

Loukanov, A. R. & Gagov, H. (2012). High-resolution subunit detection of glutamate receptor by ultrasmall gold nanoparticles, microscopy research and technique, **75**:1159–1164.

Magis, G. J., Hollander, M. J., Onderwaater, W. G., Olsen, J. D., Hunter, C. N., *et al*. (2010). Light harvesting, energy transfer and electron cycling of a native photosynthetic membrane adsorbed onto a gold surface, Biochimica et BiophysicaActa, **1798**:637–645.

Manikandan, M., Tanabe, T., Ramesh, G. V., Kodiyath, R., Ueda, S., etal. (2016). Tailoring the surface-oxygen defects of a tin dioxide support towards an enhanced electrocatalytic performance of platinum nanoparticles, Physical Chemistry and Chemical Physics, **18**:5932–5937.

Morris, L., Williams, D. E., Kaltsoyannis, N. & Tocher, D. A. (2001). Surface grafting as a route to modifying the gas-sensitive resistor properties of semiconducting oxides : Studies of Ru-grafted SnO_2, Physical Chemistry Chemical Physics, **3**:132–145.

Nancy-Xu, X. H., Huang, S., Brownlow, W., Salaita, K. & Jeffers, R. B. (2004). Size and temperature dependence of surface plasmon absorption of gold nanoparticles induced by tris(2,2-bipyridine) ruthenium(II), The Journal of Physical Chemistry B, **108**:15543–5551.

Okamoto, T. & Yamaguchi, I. (2003). Optical absorption study of the surface plasmon resonance in gold nanoparticles immobilized onto a gold substrate by self-assembly technique, The Journal of Physical Chemistry B, **107**:10321–10324.

Popescu, D. A., Herrmann, J. M., Ensuque, A. & Bozon-Verduraz, F. (2001). Nanosized tin dioxide: Spectroscopic (UV. VIS, NIR, EPR) and electrical conductivity studies, Physical Chemistry Chemical Physics, **3**:2522–2530.

Ritson, J. P., Graham, N. J. D., Templeton, M. R., Clark, J. M., Gough, R. *et al*. (2014). The impact of climate change on the treatability of dissolved organic matter (DOM) in upland water supplies: A UK perspective, Science of the Total Environment, **473–474**:714–730.

Rodriguez, P., Plana, D., Fermin, D. J. & Koper, M. T. M. (2014). New insights into the catalytic activity of gold nano-particles for CO oxidation in electrochemical media, Journal of Catalysis, **311**:182–189.

Sawada, H., Esaki, M. & Practical, A. (2000). A practical technique to postfix nanogold-immuno labeled specimens with osmium and to embed them in epon for electron microscopy, The Journal of Histochemistry and Cytochemistry, **48**:493–498.

Severin, K. G., Abdel-Fattah, T. M. & Pinnavaia,T. J. (1998). Supramolecular assembly of mesostructured tin oxide. Chemical Communications, 1471–1472.

Shaalan, N. M., Hamad, D., Abdel-Latief, A. Y. & Abdel-Rahim, M. A. (2016). Preparation of quantum size of tin oxide: Structural and physical characterization, Progress in Natural Science: Materials International, **26**:145–151.

Sing, K. S. W., Everett, D. H., Haul, R. A. W., Mouscou, L., Pierottin, R. A., *et al*. (1985). Reporting physisorption data for gas/solid systems with special reference to the determination of surface area and porosity, Pure and Applied Chemistry, **57**:603–619.

Smith, A. J., McGowan, T., Devlin, M. J., Massoud, M. S., Al-Enezi, M., *et al*. (2015). Screening for contaminant hotspots in the marine environment of Kuwait using ecotoxicological and chemical screening techniques, Marine Pollution Bulletin, **100**(2):681–688, doi.org/10.1016/j.marpolbul.2015.08.043.

Smith, A. M. & Nie, S. (2011). Bright and compact alloyed quantum dots with broadly tunable near-infrared absorption and fluorescence spectra through mercury cation exchange, Journal of American Chemical Society, **133**:24–26.

Tonezzer, M. & Hieu, N. V. (2012). Size-dependent response of single-nanowire gas sensors, Sensors and Actuators B: Chemical, **163**:146–152.

Tunstall, D.P., Patou, S., Liu, R.S. & Kao, Y.H. (1999). Size effects in the NMR of SnO_2 powders. MaterialsResearch Bulletin, **34**:1513–1520.

Uddin, M. T., Nicolas, Y., Olivier, C., Toupance, T., Servant, L., *et al*. (2012). Nanostructured SnO_2–ZnO heterojunction photocatalysts showing enhanced photocatalytic activity for the degradation of organic dyes, Inorganic Chemistry, **51**:7764–7773.

Wagner, Th., Bauer, M., Sauerwald, T. Kohl, C. D. & Tiemann, M. (2011). X-ray absorption near-edge spectroscopy investigation of the oxidation state of Pd species in nanoporous SnO_2 gas sensors for methane detection, Thin Solid Films, **520**:909–912.

Woehrle, G. H., Warner, M. G. & Hutchison, J. E. (2002). Ligand exchange reactions yield subnanometer, thiol-stabilized gold particles with defined optical transitions, Journal of Physical Chemistry B, **106**:9979–9981.

Yu, W., Jiang, K., Wu, J., Gan, J., Zhu, M., *et al*. (2011). Electronic structures and excitonic transitions in nanocrystalline iron-doped tin dioxide diluted magnetic semiconductor films: An optical spectroscopic study, Physical Chemistry Chemical Physics, **13**:6211–6222.

Zhao, Y., Dong, G., Duan, L., Qiao, J., Zhang, D., *et al*. (2012). Impacts of Sn precursors on solution-processed amorphous zinc–tin oxide films and their transistors, Royal Society of Chemistry Advances, **2**:5307–5313.

Zhang, G. & Liu, M. (2000). Effect of particle size and dopant on properties of SnO_2-based gas sensors, Sensors and Actuators B, **69**:144–152.

Submitted: 26/12/2016
Revised : 17/05/2017
Accepted : 28/05/2017

طريقه مبتكره في صناعه ثاني أكسيد القصدير البلوري والميزومسامي يحتوي على حبيبات ذهب نانومتريه

تأليف طارق عقيل[1*] و هذر جرير[2] وعلي بومجداد[3]

1*- قسم العلوم في كليه التربيه الأساسية بالهيئه العامه للتعليم التطبيقي والتدريب ص ب 23167 الرمز البريدي 13092 الصفات – الكويت

المؤلف المراسل: tm.aqeel@paaet.edu.kw*

الملخص

لقد قمنا بصناعه ثاني أكسيد القصدير البلوري الميزو مسامي المرصع بحبيبات الذهب النانومتري بطريقه مبتكره

باستخدام الطريقه المباشره للقوالب الطريه تحت الضغط الجوي السائد. كما قمنا بتشخيص والتعرف على مكونات السطحيه والتركيب الأساسي وخواص هذه الماده الجديده باستخدام الفحوصات التاليه: فحص المساميه لبرنرد\أميت\تلر وفحص أشعه أكس المتشتته والحيود والفلوروسنتيه والمكبر الالكتروني عالي الدقه والاشعه المرئيه\والفوق بنفسجيه.

وقد أثبتت هذه الفحوصات أن الماده الجديده تحتوي على مساحه سطحيه عاليه 97 متر لكل جرام ونطاق ضيق من المسامات يقع بين 3-2 نانومتر. كما نعتقد أن حبيبات الذهب انحشرت بالبدايه بالمسام مما حد من تجمعها عند تحضيرها ثم تغلغلت الى حوائط ثاني أكسيد القصدير أثناء تعرضها للمعالجه الحراريه الثانيه. وكان متوسط قياس حبيبات الذهب يقارب 1 نانوميتر وهذا يبين أن بهذه الطريقه المبتكره يمكننا السيطره على قياس الحبيبات المتكونه وايضا قياس المسام بالماده الأم. وأيضا قمنا بتحديد وقياس الفجوه الحزميه لهذه الماده بطريقه كبيلكا- منك وهي تساوي 3 اليكترون فولت. وأيضا قمنا بقياس الحساسيه الضوئيه لهذه الماده الجديده مقارنتا بالماده الأم (ثاني اكسيد القصدير الميزومسامي) فوجدنا أن المادتين لهما نشاط كهروضوئي تحت تأثير الضوء المرئي والأشعه الفوق بنفسجيه و يتأثران أكثر بالأشعه الفوق بنفسجيه كما تبين أن نشاط الكهروضوئي للماده الجديده يفوق نشاط الماده الأصليه بمئات المرات.